

Article

Synthesis of Core-Shell Carbon Encapsulated Fe₂O₃ Composite through a Facile Hydrothermal Approach and Their Application as Anode Materials for Sodium-Ion Batteries

Yongguang Zhang ¹, Zhumabay Bakenov ² , Taizhe Tan ^{1,*} and Jin Huang ^{1,*}

¹ School of Materials and Energy, Synergy Innovation Institute of GDUT, Guangdong University of Technology, Guangzhou 510006, China; ygzhang126@126.com

² Institute of Batteries LLC, School of Engineering, National Laboratory Astana, Nazarbayev University, 53 Kabanbay Batyr Avenue, Astana 010000, Kazakhstan; zbakeno@nu.edu.kz

* Correspondence: tztansii18@163.com (T.T.); huangjiner@126.com (J.H.)

Received: 24 May 2018; Accepted: 15 June 2018; Published: 18 June 2018



Abstract: Carbon encapsulated Fe₂O₃ nanoparticles (C@Fe₂O₃) were successfully synthesized via a facile and environmentally friendly hydrothermal method and prototyped in anode materials for sodium ion batteries (SIBs). High-resolution transmission and scanning electronic microscopy observations exhibited the formation of a highly core-shelled C@Fe₂O₃ composite consisting of carbon layers coated onto uniform Fe₂O₃ nanoparticles with a median diameter of 46.1 nm. This core-shell structure can repress the aggregation of Fe₂O₃ nanoparticles, preventing the harsh volume change of the electrode, enhancing the electric conductivity of the active materials, and promoting Na-ion transformation during cycling. The electrochemical performances of the C@Fe₂O₃ composite, as anodes for SIBs, retained a reversible capacity of 305 mAh g⁻¹ after 100 cycles at 50 mA g⁻¹ and exhibited an excellent cyclability at various current densities due to the synergistic effect between the carbon layers and Fe₂O₃. These results suggest that C@Fe₂O₃ composites present much potential as anode materials for rechargeable SIBs.

Keywords: C@Fe₂O₃ composite; anode; sodium ion battery

1. Introduction

Recently, sodium-ion batteries (SIBs) have attracted intensive attention as an alternative to lithium-ion batteries (LIBs). This interest can be attributed to the fact that sodium is abundantly available and is economically cheaper than lithium [1,2]. Graphite was established as the gold-standard anode material for lithium ion batteries (LIBs) due to their modest reversible capacity (372 mAh g⁻¹), superior cycling behavior, high Coulombic efficiency, low cost, and low and flat potential plateaus, which provide a decent voltage window [3]. However, conventional graphite is not suitable for SIB anodes because the larger atomic radius of sodium requires intercalation hosts, with larger diffusion channels [4]. In recent years, the researched anode materials for SIBs transition metal oxides, such as TiO₂, ZnO, and Co₃O₄, were found to hold the greatest potential for anode materials in SIBs due to their exceptional theoretical capacities, good versatility, and cost advantages [5–10]. In general, these anodes face severe challenges in poor electronic conductivity and huge volume changes during cycling. Therefore, the development of anode materials with excellent electrochemical performances is crucial. In particular, Fe₂O₃, which possess a lofty theoretical specific capacity (1007 mAh g⁻¹) [11], has garnered much attention in recent years [8–11]. However, the cycling stability of the Fe₂O₃ anode is significantly hindered by the harsh volume expansion/contraction during the Na alloying/dealloying

processes. To boost the stability of the Fe_2O_3 anode and better the capacity retention and cycle life, an effective strategy, which has been previously investigated, is to combine Fe_2O_3 nanoparticles with carbonaceous substances. For example, Wang's group reported the preparation of $\alpha\text{-Fe}_2\text{O}_3/\text{RGO}$ composites via microwave autoclave, with the resulting nanocomposites delivering a capacity of 310 mAh g^{-1} after 150 cycles at 100 mA g^{-1} [12].

In lithium-ion batteries, the carbon encapsulated Fe_2O_3 nanoparticles ($\text{C@Fe}_2\text{O}_3$) as anode materials attract special interest of researchers since this core-shell structured nanocomposite exhibits enhanced physical and chemical properties [13]. Coating layers of carbon onto a Fe_2O_3 core will simultaneously improve the electric conductivity and act as a buffer layer to mitigate the mechanical strain and improve the mechanical integrity due to the ductile and elastic nature of carbonaceous materials [14,15]. All these merits are beneficial for the development of electrochemical performance. Encouraged by these promising and interesting works, herein, we prepared core-shell structure $\text{C@Fe}_2\text{O}_3$ composites by a one-step hydrothermal procedure. Carbon layers were homogeneously coated on the Fe_2O_3 nanoparticles, with a median diameter of 46.1 nm. From this unique design, the $\text{C@Fe}_2\text{O}_3$ composites exhibit an impressive Na-ion storage performance with a high capacity and good cycles.

2. Materials and Methods

2.1. Materials Preparation

The $\text{C@Fe}_2\text{O}_3$ composites with a core-shell structure were synthesized by the hydro-thermal method. Glucose (0.3 g) and iron nitrate hydrate (0.4 g) were dispersed in distilled water (40 mL) using a thermostatic magnetic mixer (Zhengzhou Teer Instruments, Zhengzhou, China) for 0.5 h to form a uniform suspension. Subsequently, the mixed solution was displaced to reaction still after 0.25 h sonication using an ultrasonic cell disruptor (Ningbo Scientz Biotechnology Co., Ningbo, China), then heated in a 40 mL Teflon-lined stainless-steel autoclave for 9 h at $190 \text{ }^\circ\text{C}$, and then left in ambient conditions. After cooling to room temperature, the products were washed thoroughly via centrifugal with deionized water. Finally, the washed products were dried under vacuum at $80 \text{ }^\circ\text{C}$ for 24 h to prepare carbon encapsulated Fe_2O_3 nanoparticles in a core-shell structure.

2.2. Materials Characterization

The crystal phase of $\text{C@Fe}_2\text{O}_3$ composites was analyzed by Rigaku D/Max 2500V/pc X-ray diffractometer (XRD) (Rigaku-TTRIII, Tokyo, Japan) with $\text{Cu K}\alpha$ ($\lambda = 1.5406 \text{ \AA}$) in scanning step of 0.02° . The morphology was observed by a JEOL JSM-6700F scanning electron microscope (SEM, equipped with EDX elemental analysis, JEOL, Tokyo, Japan) and high-resolution transmission electron microscopy (HR-TEM, JEOL, Tokyo, Japan) from a JEOL JEM-2100F instrument with 200 kV acceleration voltage. Brunauer Emmett Teller (BET) (V-Sorb 2800P) tests were conducted to investigate the specific surface area of the composites. X-ray photoelectron spectroscopy (XPS) data was obtained with a PHI 5000 Versa Probe system (Ulvac-Phi, Kanagawa, Japan). The carbon content was estimated by thermo gravimetric analysis (TGA, SDTQ600, TA Instruments-Waters LLC, Newcastle, PA, USA). Raman spectroscopy analysis was examined on Raman spectroscopy (LabRAM Hr 800, HORIBA Jobin Yvon, Paris, France) with the laser wavelength of 514 nm.

2.3. Electrochemical Measurements

The electrochemical measurements were conducted at room temperature using coin cells (CR2025), with a sodium foil as the counter and reference electrode. The working electrode consisted of a $\text{C@Fe}_2\text{O}_3$ slurry, acetylene black, and sodium alginate binder combined at a weight ratio, 7:2:1, and evenly applied onto copper foil with 15 mm in diameter. The as-prepared working electrodes were dried in a vacuum oven at $80 \text{ }^\circ\text{C}$ for over 12 h to remove any residual moisture. The electrolyte was comprised of 1 M NaClO_4 dissolved in a mixture of ethylene carbonate and dimethyl carbonate (1:1 by volume),

and the separator used was a glass fiber film. The electrochemical performances were probed between 0.01 and 3.0 V (vs. Na/Na⁺) with a battery testing system (BTS-5V5 mA, Neware, Shenzhen, China). The specific capacity was calculated in reference to the mass of the total active material.

3. Results and Discussion

The crystalline structure of the C@Fe₂O₃ composite was characterized by XRD. Figure 1 shows that the typical diffraction peaks at 30.3°, 35.7°, 57.4°, and 63.1°, which correspond to the reflections of (2 0 6), (1 1 9), (1 1 15), and (4 0 12) planes of the Fe₂O₃ structure (JCPDS No. 25-1402), respectively. There is no evident carbon peak due to the presence of amorphous carbon.

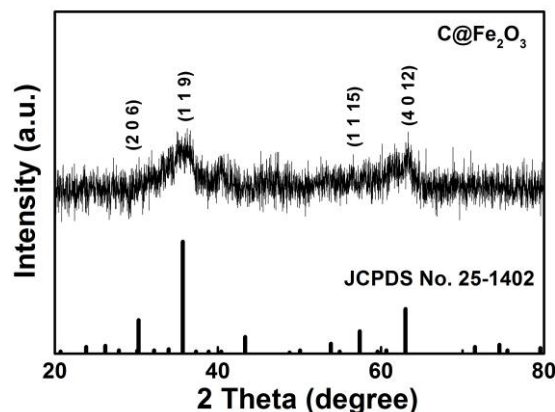


Figure 1. X-ray diffractometer (XRD) patterns of the C@Fe₂O₃ composite.

Raman spectra further confirmed the presence of carbon in the composites. As shown in Figure 2, two obvious bands at 1350 and 1586 cm⁻¹ are assigned to typical D and G bands of carbon, respectively. A 2D band of 2693 cm⁻¹ is also observed, confirming the presence of carbon from the hydro-thermal process of glucose in the composites.

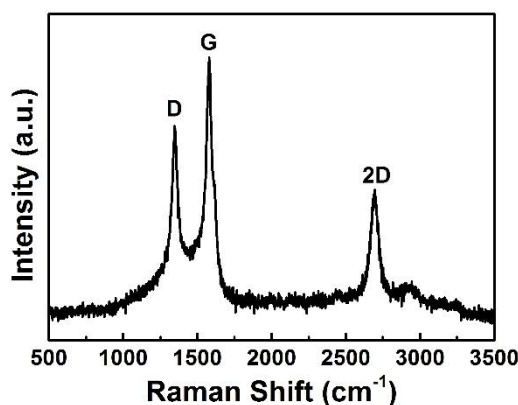


Figure 2. Raman spectrum of the C@Fe₂O₃ composite.

The morphology and particle sizes of C@Fe₂O₃ composites were characterized by SEM measurements. As shown in Figure 3a,b, the C@Fe₂O₃ composites are uniform spheres, with a median diameter of approximately 50 nm. The inset in Figure 3b depicts the average diameter of the C@Fe₂O₃ composites was 46.1 nm. The structure of the C@Fe₂O₃ composite was further investigated by TEM. Figure 3c illustrates carbon wrapping of Fe₂O₃ nanoparticles, which possess an average diameter of ~10 nm, confirming a core-shell structure. The HRTEM analysis, shown in Figure 3d, reveals the lattice fringe, with a distance spacing of 0.238 nm, corresponding to the (2 2 6) plane of Fe₂O₃. The image also

illustrates that the thickness of the carbon layer was approximately 0.83 nm. The energy dispersive spectrometer (EDS) element mapping, shown in Figure 4, clearly demonstrates that the C@Fe₂O₃ composite mainly consist of C, Fe, and O, with a uniform distribution.

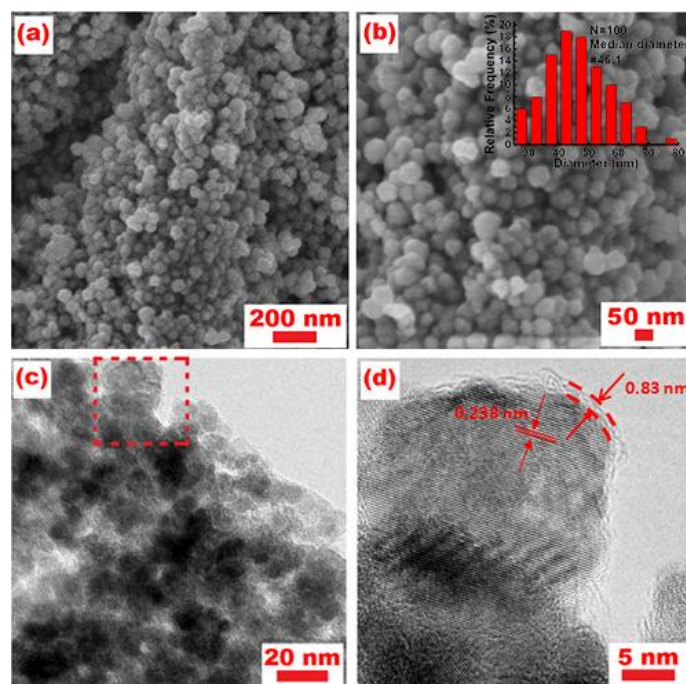


Figure 3. SEM images (a,b) and corresponding median diameter (inset) and TEM images (c,d) of the C@Fe₂O₃ composites.

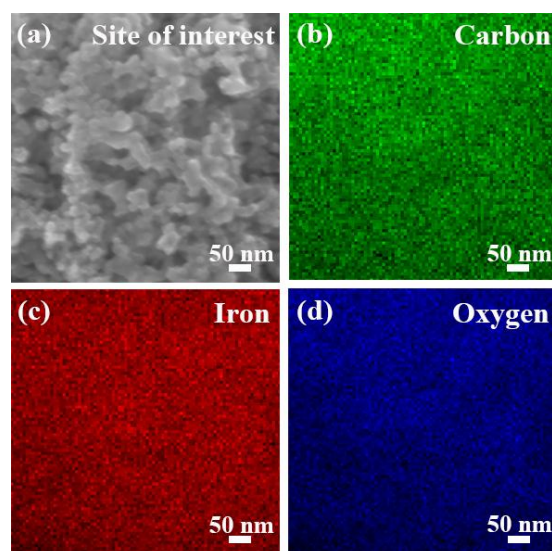


Figure 4. SEM image (a) of the C@Fe₂O₃ composite and corresponding carbon (b), iron (c), and oxygen (d) element mapping.

The chemical composition and chemical bonding were further investigated by XPS, shown in Figure 5. As shown in Figure 5a, the peaks of Fe 2p, C 1s, and O 1s were detected in the C@Fe₂O₃ composite. Figure 5b delivers two peaks located at 724.7 and 711.1 eV in the high-resolution Fe 2p spectra, corresponding to Fe 2p_{1/2} and Fe 2p_{3/2}, respectively. In addition, two weak satellite peaks at 733.3 and 719.5 eV can be attributed to the Fe 2p_{1/2} and Fe 2p_{3/2}, respectively. This phenomenon

indicates that the composite was composed of Fe^{3+} only. Figure 5c shows three peaks at 288.6, 286.6, and 284.8 eV in the C 1s spectra, corresponding to the C=O, C–O–C, and C–C, respectively. Figure 5d shows two peaks located at 531.8 and 529.8 eV in the O 1s spectra, which is attributed to Fe–O–H and Fe–O, respectively. Overall, the results indicate the successful transformation of glucose and iron nitrate hydrate into $\text{C@Fe}_2\text{O}_3$ composite.

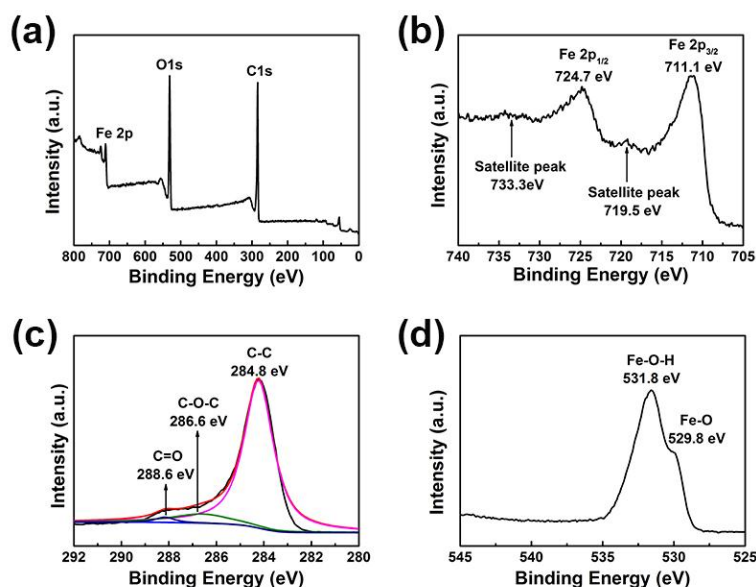


Figure 5. XPS full spectra (a), Fe 2p (b), C 1s (c), and (d) O 1s of the $\text{C@Fe}_2\text{O}_3$ composite.

The carbon content of the $\text{C@Fe}_2\text{O}_3$ composites was tested by thermogravimetric (TG) analysis. From the TG curve in Figure 6, the weight fraction of the carbon was recorded to be 46%. The specific surface area and pore size distribution of the $\text{C@Fe}_2\text{O}_3$ composite was obtained from nitrogen adsorption-desorption measurements. From Figure 7a, the isotherms indicate type IV hysteresis loops, with a marked hysteric loop in a desorption branch between relative pressures P/P_0 of 0.8 and 0.95, corresponding to the mesoporous nature of the sample. In general, the type IV hysteresis loop typically occurs due to the aggregated nanoparticle structure. The BET surface area for the $\text{C@Fe}_2\text{O}_3$ composite was calculated at $85.56 \text{ m}^2 \text{ g}^{-1}$. Figure 7b shows the Barrett-Joyner-Halenda (BJH) pore size adsorption plot for $\text{C@Fe}_2\text{O}_3$ sample, highlighting a bimodal-pore size centered at 3.7 nm and 49.9 nm. This further confirms the mesoporous morphology of $\text{C@Fe}_2\text{O}_3$ composites.

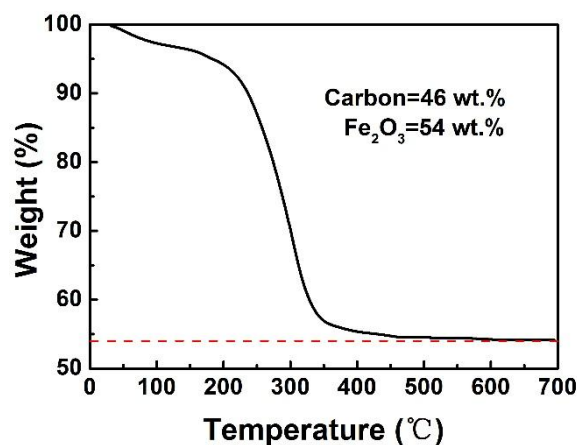


Figure 6. Thermogravimetric (TG) curve of the $\text{C@Fe}_2\text{O}_3$ composite.

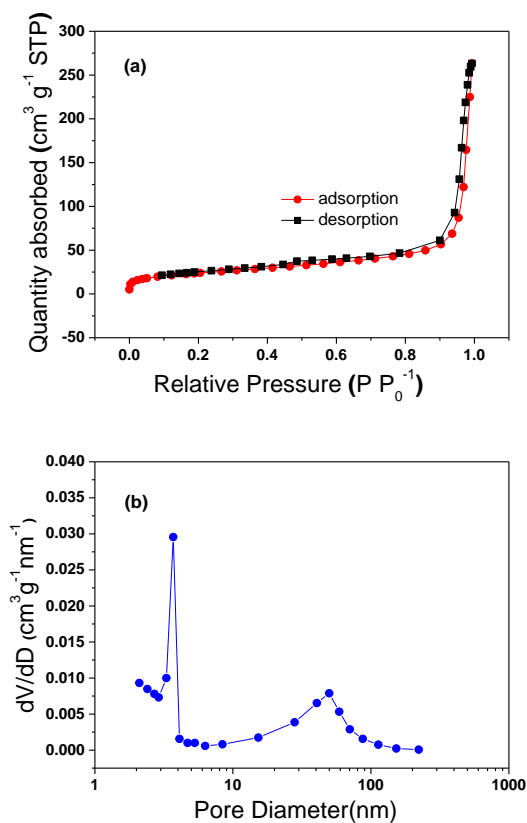


Figure 7. (a) Nitrogen adsorption/desorption isotherms and (b) the pore size distributions of C@Fe₂O₃ composites.

The electrochemical behavior of the C@Fe₂O₃ composite with Na-ion insertion-extraction was tested by cyclic voltammetry (CV) analysis as shown in Figure 8. In the cathodic scan, an irreversible peak is observed at around 0.75 V (vs. Na/Na⁺), corresponding to the formation of a solid electrolyte interface (SEI) layer [16]. The pronounced reduction peak occurs near 0.08 V, which results in the reduction of the Fe₂O₃ [17]. In the anodic scan, two broad oxidation peaks are located at 0.46 V and 1.71 V, corresponding to the reversible oxidation of Fe⁰ to Fe³⁺ [18]. The reversible electrochemical reaction can be described as [19]:

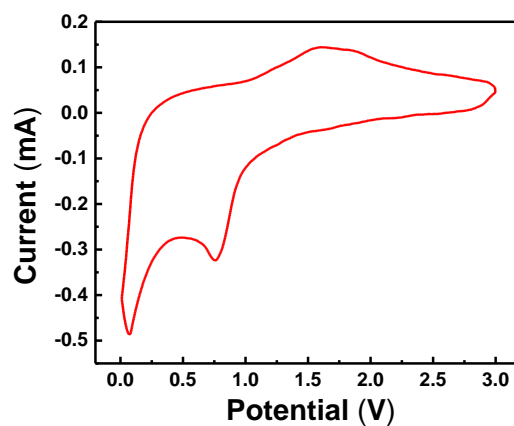
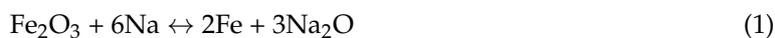


Figure 8. Cyclic voltammetry (CV) curve of the C@Fe₂O₃ composite at the initial cycle.

Figure 9 illustrates the charge–discharge profiles for the initial three cycles of the C@Fe₂O₃ composites at a current density of 50 mA g^{−1} and at a potential window between 0.01 and 3.0 V. As observed, the C@Fe₂O₃ composite delivers an initial discharge capacity of 709 mAh g^{−1} and a charge capacity of 415 mAh g^{−1}, which mainly originates in the first cycle, partially from the inevitable formation of the SEI film on the surface of the C@Fe₂O₃ electrode and the unique core-shell structure, which possesses a high specific surface area [20]. SEI films are generated from the decomposition of electrolyte, which produces a large amount of sodium ions and irreversibly intercalate into the crystal lattice [21]. In addition, no obvious voltage plateaus can be observed in Figure 9, which is accepted of Fe₂O₃ as is reported in the literature. Lastly, the capacity of the C@Fe₂O₃ composite quickly faded in the subsequent cycles because of the drastic volume change and the aggregation of Fe₂O₃ nanoparticles during charge–discharge processes [22].

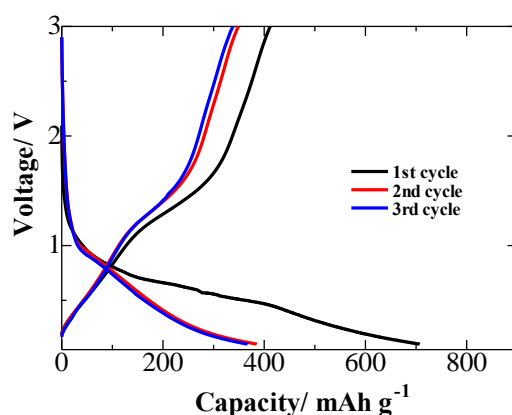


Figure 9. The charge-discharge profiles of the C@Fe₂O₃ composites at the initial three cycles at 50 mA g^{−1} between 0.01 and 3.0 V.

At a current density of 50 mA g^{−1} for 100 cycles, the cycling performances of C@Fe₂O₃ composite are shown in Figure 10. In the first cycle, the C@Fe₂O₃ composite manifests a high irreversible discharge capacity of 709 mAh g^{−1} and a relatively low initial coulombic efficiency of less than 60%. Subsequently, excellent cycle performance is maintained delivering a reversible capacity of 305 mAh g^{−1} for 100 cycles. Furthermore, along with a high reversible discharge capacity, excellent cyclability was demonstrated as well, and the capacity decay was only 0.22% in per cycle. Complimentarily, the C@Fe₂O₃ electrode delivers a coulombic efficiency of over 99%. In summary, these results imply an excellent reversibility of sodium insertion/deinsertion in the C@Fe₂O₃ composites.

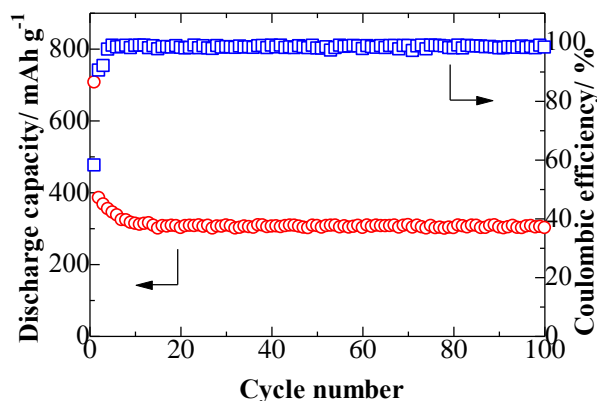


Figure 10. Cycling performance and coulombic efficiency of the C@Fe₂O₃ composites.

Figure 11 exhibits the rate capabilities of the C@Fe₂O₃ composite electrode at different current densities, spanning from 50 mA g⁻¹ to 1000 mA g⁻¹. The C@Fe₂O₃ composite electrode demonstrates excellent rate performance and reversible capacities of 364, 291, 245, 206, and 150 mAh g⁻¹ at current densities of 50, 100, 200, 500, and 1000 mA g⁻¹, respectively. Lastly, the C@Fe₂O₃ composite delivered a reversible capacity of 302 mAh g⁻¹ when returning the current density back to the initial 50 mA g⁻¹. These results reveal that the stable core-shell structure of the carbon encapsulated Fe₂O₃ nanoparticles can effectively sustain the large volume change, alleviate the aggregation of Fe₂O₃ nanoparticles, and improve electronic transports during sodium insertion [16,23,24].

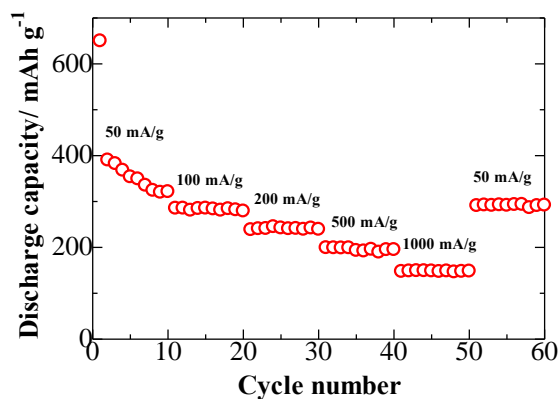


Figure 11. Rate performances of the C@Fe₂O₃ composites at various current densities.

Electrochemical impedance spectroscopy (EIS) measurements were measured to compare the Nyquist plots of C@Fe₂O₃ when fresh and after 100 cycles, as shown in Figure 12. The C@Fe₂O₃ composite, after 100 cycles, had much lower charge transfer resistance, corresponding to the smaller semicircle at high to middle frequency. As a result, the C@Fe₂O₃ composite exhibits a favorable electrochemical performance during cycling processes.

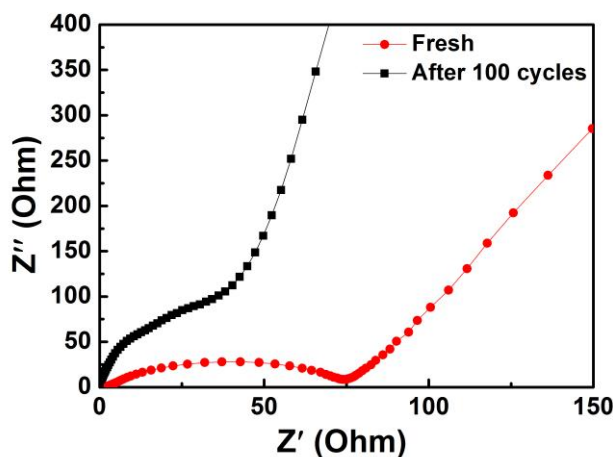


Figure 12. Impedance plots of the C@Fe₂O₃ composite when fresh and after 100 cycles.

The electrochemical performance of C@Fe₂O₃ composites obtained in this paper is better than those of previously reported results with Fe₂O₃ (Table 1) [12,25]. Compared with Fe₂O₃, the cycling performance of the C@Fe₂O₃ composites is much better, showing that the carbon contributes to the capacity of the C@Fe₂O₃ composites and the carbon is taking a positive effect.

Table 1. Comparison of the electrochemical performances of Fe₂O₃ and C@Fe₂O₃ composite for sodium-ion batteries.

Materials	Discharge Capacity (mAh g ⁻¹)	Cycle Number	Current Density (mAh g ⁻¹)	References
Fe ₂ O ₃	16	10	50	[25]
α-Fe ₂ O ₃	10	50	100	[12]
C@Fe ₂ O ₃	305	100	50	This study

4. Conclusions

In summary, we reported a facile hydrothermal approach to fabricate a stable core-shell structure composed of carbon encapsulated Fe₂O₃ nanoparticles and investigated its application as anode materials for SIBs. A reversible capacity of 305 mAh g⁻¹ can be obtained at 50 mA g⁻¹ for up to 100 cycles for the C@Fe₂O₃ composites and it delivered a reversible capacity of 150 mAh g⁻¹ at a current density of 1000 mA g⁻¹. When the current rate returned to 50 mA g⁻¹, the reversible capacity could recover up to 302 mAh g⁻¹, indicating high rate capabilities even at very high current densities. The electrochemical results demonstrated that the C@Fe₂O₃ composites feature excellent cycling performance and good rate capability due to the unique core-shell structure of the SIB anode.

Author Contributions: Formal Analysis, Y.Z.; Investigation, Y.Z.; Writing-Original Draft Preparation, T.T. and Y.Z.; Writing-Review & Editing, Z.B. and J.H.; Supervision, J.H.; Project Administration, T.T.; Funding Acquisition, Y.Z.

Funding: This research was funded by the China Postdoctoral Science Foundation (2018M630924); Program for the Outstanding Talents of Guangdong sailing plan, Human Resources and Social Security of Guangdong Province (201634007). ZB acknowledges support from a research project by the Ministry of Education and Science “Zinc based Rechargeable Aqueous Battery: A green, safe and economic battery for Space Applications” (AP05136016).

Conflicts of Interest: The authors declare no conflict of interest.

References

1. Firouzi, A.; Qiao, R.M.; Motallebi, S.; Valencia, C.W.; Israel, H.S.; Fujimoto, M.; Wray, L.A.; Chuang, Y.D.; Yang, W.L.; Wessells, C.D. Monovalent manganese based anodes and co-solvent electrolyte for stable low-cost high-rate sodium-ion batteries. *Nat. Commun.* **2018**, *9*, 861. [[CrossRef](#)] [[PubMed](#)]
2. Yuan, G.H.; Xiang, J.M.; Jin, H.F.; Jin, Y.Z.; Wu, L.Z.; Zhang, Y.G.; Mentbayeva, A.; Bakenov, Z. Flexible free-standing Na₄Mn₉O₁₈/reduced graphene oxide composite film as a cathode for sodium rechargeable hybrid aqueous battery. *Electrochim. Acta* **2018**, *259*, 647–654. [[CrossRef](#)]
3. Li, H.P.; Wei, Y.Q.; Zhang, Y.G.; Zhang, C.W.; Wang, G.K.; Zhao, Y.; Yin, F.X.; Bakenov, Z. In situ sol-gel synthesis of ultrafine ZnO nanocrystals anchored on graphene as anode material for lithium-ion batteries. *Ceram. Int.* **2016**, *42*, 12371–12377. [[CrossRef](#)]
4. Willis, T.J.; Porter, D.G.; Voneshen, D.J.; Uthayakumar, S.; Demmel, F.; Gutmann, M.J.; Roger, M.; Refson, K.; Goff, J.P. Diffusion mechanism in the sodium-ion battery material sodium cobaltate. *Sci. Rep.* **2018**, *8*, 3210. [[CrossRef](#)] [[PubMed](#)]
5. Chen, C.M.; Yang, Y.C.; Ding, S.S.; Wei, Z.X.; Tang, X.; Li, P.C.; Wang, T.H.; Cao, G.Z.; Zhang, M. S-doped carbon@TiO₂ to store Li⁺/Na⁺ with high capacity and long life-time. *Energy Storage Mater.* **2018**, *13*, 215–222. [[CrossRef](#)]
6. Teng, Y.Q.; Mo, M.S.; Li, Y.; Xue, J.L.; Zhao, H.L. Amorphous carbon-coated ZnO porous nanosheets: Facile fabrication and application in lithium- and sodium-ion batteries. *J. Alloys Compd.* **2018**, *744*, 712–720. [[CrossRef](#)]
7. Sultana, I.; Rahman, M.M.; Materi, S.; Ghanooni, A.V.; Glushenkov, A.M.; Chen, Y. K-ion and Na-ion storage performances of Co₃O₄-Fe₂O₃ nanoparticle-decorated super P carbon black prepared by a ball milling process. *Nanoscale* **2017**, *9*, 3646–3654. [[CrossRef](#)] [[PubMed](#)]
8. Fiore, M.; Longoni, G.; Santangelo, S.; Pantò, F.; Stelitano, S.; Frontera, P.; Antonucci, P.; Ruffo, R. Electrochemical characterization of highly abundant, low cost iron (III) oxide as anode material for sodium-ion rechargeable batteries. *Electrochim. Acta* **2018**, *269*, 367–377. [[CrossRef](#)]

9. Meng, S.; Zhao, D.L.; Wu, L.L.; Ding, Z.W.; Cheng, X.W.; Hu, T. Fe₂O₃/nitrogen-doped graphene nanosheet nanocomposites as anode materials for sodium-ion batteries with enhanced electrochemical performance. *J. Alloys Compd.* **2018**, *737*, 130–135. [[CrossRef](#)]
10. Liu, Y.C.; Wang, F.F.; Fan, L.Z. Self-standing Na-storage anode of Fe₂O₃ nanodots encapsulated in porous N-doped carbon nanofibers with ultra-high cyclic stability. *Nano Res.* **2018**, *1*, 1–12. [[CrossRef](#)]
11. Jiang, Y.; Hu, M.; Zhang, D.; Yuan, T.; Sun, W.; Xu, B.; Yan, M. Transition metal oxides for high performance sodium ion battery anodes. *Nano Energy* **2014**, *5*, 60–66. [[CrossRef](#)]
12. Zhang, Z.J.; Wang, Y.X.; Chou, S.L.; Li, H.J.; Liu, H.K.; Wang, J.Z. Rapid synthesis of α -Fe₂O₃/rGO nanocomposites by microwave autoclave as superior anodes for sodium-ion batteries. *J. Power Sources* **2015**, *280*, 107–113. [[CrossRef](#)]
13. Gao, G.; Yu, L.; Wu, H.B.; Lou, X.W. Hierarchical tubular structures constructed by carbon-coated α -Fe₂O₃ nanorods for highly reversible lithium storage. *Small* **2014**, *10*, 1741–1745. [[CrossRef](#)] [[PubMed](#)]
14. Li, H.P.; Li, Y.; Zhang, Y.G.; Zhang, C.W. Facile synthesis of carbon-coated Fe₃O₄ core-shell nanoparticles as anode materials for lithium-ion batteries. *J. Nanopart. Res.* **2015**, *17*, 370. [[CrossRef](#)]
15. Zhang, Y.G.; Li, Y.; Li, H.P.; Zhao, Y.; Yin, F.X.; Bakenov, Z. Electrochemical performance of carbon-encapsulated Fe₃O₄ nanoparticles in lithium-ion batteries: Morphology and particle size effects. *Electrochim. Acta* **2016**, *216*, 475–483. [[CrossRef](#)]
16. Jian, Z.L.; Zhao, B.; Liu, P.; Li, F.J.; Zheng, M.B.; Chen, M.W.; Shi, Y.; Zhou, H.S. Fe₂O₃ nanocrystals anchored onto graphene nanosheets as the anode material for low-cost sodium-ion batteries. *Chem. Commun.* **2014**, *50*, 1215–1217. [[CrossRef](#)] [[PubMed](#)]
17. Zhang, N.; Han, X.; Liu, Y.; Hu, X.; Zhao, Q.; Chen, J. 3D porous γ -Fe₂O₃@C nanocomposite as high-performance anode material of Na-ion batteries. *Adv. Energy Mater.* **2015**, *5*, 1401123–1401130. [[CrossRef](#)]
18. Wu, Z.G.; Zhong, Y.J.; Liu, J.; Wu, J.H.; Guo, X.D.; Zhong, B.H.; Zhang, Z.Y. Subunits controlled synthesis of α -Fe₂O₃ multi-shelled core-shell microspheres and their effects on lithium/sodium ion battery performances. *J. Mater. Chem. A* **2015**, *3*, 10092–10099. [[CrossRef](#)]
19. Philippe, B.; Valvo, M.; Lindgren, F.; Rensmo, H.; Edstrom, K. Investigation of the Electrode/Electrolyte Interface of Fe₂O₃ Composite Electrodes: Li vs Na Batteries. *Chem. Mater.* **2014**, *26*, 5028–5041. [[CrossRef](#)]
20. Wang, S.B.; Wang, W.; Zhan, P.; Jiao, S.Q. Hollow α -Fe₂O₃ nanospheres synthesized using a carbon template as novel anode materials for Na-ion batteries. *ChemElectroChem* **2014**, *1*, 1636–1639. [[CrossRef](#)]
21. Valvo, M.; Lindgren, F.; Lafont, U. Towards more sustainable negative electrodes in Na-ion batteries via nanostructured iron oxide. *J. Power Sources* **2014**, *245*, 967–978. [[CrossRef](#)]
22. Xu, X.; Cao, R.; Jeong, S.; Cho, J. Spindle-like mesoporous α -Fe₂O₃ anode material prepared from MOF template for high-rate lithium batteries. *Nano Lett.* **2012**, *12*, 4988–4991. [[CrossRef](#)] [[PubMed](#)]
23. Su, D.W.; Ahn, H.J.; Wang, G.X. SnO₂@graphene nanocomposites as anode materials for Na-ion batteries with superior electrochemical performance. *Chem. Commun.* **2013**, *49*, 3131–3133. [[CrossRef](#)] [[PubMed](#)]
24. Wang, W.; Hu, L.W.; Ge, J.B.; Hu, Z.Q.; Sun, H.B.; Sun, H.; Zhang, H.Q.; Zhu, H.M.; Jiao, S.Q. In situ self-assembled FeWO₄/graphene mesoporous composites for Li-ion and Na-ion batteries. *Chem. Mater.* **2014**, *26*, 3721–3730. [[CrossRef](#)]
25. Liu, X.J.; Chen, T.Q.; Chu, H.P.; Niu, L.Y.; Sun, Z.; Pan, L.K.; Sun, C.Q. Fe₂O₃-reduced graphene oxide composites synthesized via microwave-assisted method for sodium ion batteries. *Electrochim. Acta* **2015**, *166*, 12–16. [[CrossRef](#)]

